Control of Structural Distortions in Transition-Metal Oxide Films through Oxygen Displacement at the Heterointerface

Ryotaro Aso, Daisuke Kan, Yuichi Shimakawa, and Hiroki Kurata**

Structural distortions in the oxygen octahedral network in transition-metal oxides play crucial roles in yielding a broad spectrum of functional properties, and precise control of such distortions is a key for developing future oxide-based electronics. Here, it is shown that the displacement of apical oxygen atom shared between the octahedra at the heterointerface is a determining parameter for these distortions and consequently for control of structural and electronic phases of a strained oxide film. The present analysis by complementary annular dark- and bright-field imaging in aberration-corrected scanning transmission electron microscopy reveals that structural phase differences in strained monoclinic and tetragonal $SrRuO_3$ films grown on $GdScO_3$ substrates result from relaxation of the octahedral tilt, associated with changes in the in-plane displacement of the apical oxygen atom at the heterointerface. It is further demonstrated that octahedral distortions and magnetrotransport properties of the $SrRuO_3$ films can be controlled by interface engineering of the oxygen displacement. This provides a further degree of freedom for manipulating structural and electronic properties in strained films, allowing the design of novel oxide-based heterostructures.

1. Introduction

A wide variety of functional properties seen in ABO_3 perovskite-structure transition-metal oxides are often underpinned by slight structural distortions in an ideal three-dimensional framework of corner-connected oxygen octahedra, BO_6.[1–13] The framework structure can accommodate octahedral deformations (changes in size), cooperative tilting (or rotations), and cation displacements. Control of such structural distortions and ultimately engineering of functional properties in these oxides by external means is of great importance and a central research topic in fundamental materials science and in applications of oxide materials in electronic devices. Heterointerfaces consisting of dissimilar oxides have been intensively investigated and have been recognized as a good platform to explore the capability to control the distortions and engineer their properties.[14–21] At such interfaces, the in-plane lattice spacing of the two oxides is required to match (the so-called strain effect), resulting in modifications of the octahedral deformations and tilts, which impact the properties. Recent theoretical studies have shown that besides the strain effect, the interfacial connection between the BO_6 octahedra with different tilt patterns and angles is crucial for structural and functional properties.[22–27] However, characterizing changes in the oxygen octahedral deformation and tilt across the heterointerface has been a big experimental challenge, and the corresponding effects on properties have not been clarified yet.

Recently, we demonstrated that high-resolution high-angle annular dark-field (HAADF) and annular bright-field (ABF) imaging in aberration-corrected scanning transmission electron microscopy (STEM) allow us to determine the precise atomic positions of all constituent atoms, including oxygen, across a heterointerface.[14] With this technique, we revealed that even in a strained film, wherein the in-plane lattice spacing is identical to that of the substrate, there are some degrees of freedom of the oxygen atomic positions, namely the octahedral tilt angle. This implies that the oxygen atoms comprising the octahedra play a critical role in accommodating the strain energy associated with octahedral distortions due to matching of the in-plane lattice parameters and octahedral connection angles at the interface. This raises another possibility that different types of distortions can be introduced and manipulated in the octahedral framework by adjusting the oxygen atomic positions.

This study focuses on $SrRuO_3$ (SRO) thin films with +1.0% tensile strain grown on (110) $GdScO_3$ (GSO) substrates. Previously, we found that SRO films undergo a structural phase transition from a distorted-orthorhombic (monoclinic) structure for film thickness below 16 nm to a tetragonal structure above this thickness.[2] X-ray structure characterizations showed that upon the structural phase transition, there was no difference in the in-plane lattice spacing, suggesting that the transition is driven by changes in the oxygen octahedral tilt in the strained films.

Here, we present high-resolution HAADF- and ABF-STEM observations of SRO films to track changes in oxygen atomic positions upon this structural phase transition. The observations revealed that the structural transition originates

R. Aso, Dr. D. Kan, Prof. Y. Shimakawa, Prof. H. Kurata
Institute for Chemical Research
Kyoto University
Uji, Kyoto 611–0011, Japan
E-mail: dkan@scl.kyoto-u.ac.jp
kurata@eels.kuicr.kyoto-u.ac.jp
Prof. Y. Shimakawa, Prof. H. Kurata
Japan Science and Technology Agency
CREST, Uji, Kyoto 611–0011, Japan

DOI: 10.1002/adfm.201303521

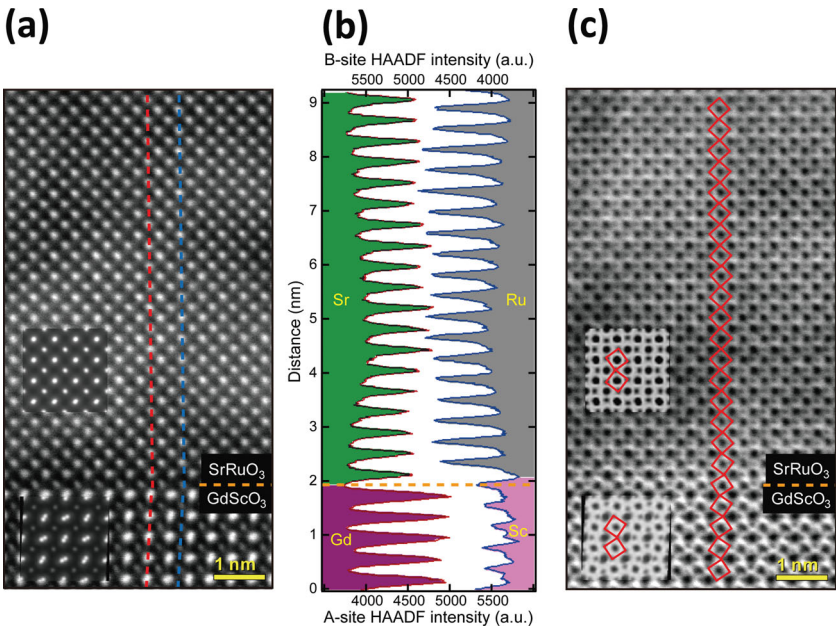

Figure 1. High-resolution cross-sectional HAADF- and ABF-STEM images of SRO/GSO heterostructure and element characterization. a) High-resolution HAADF image of the 23 nm-thick tetragonal SRO thin film grown on the GSO substrate taken along the $[001]_{ortho}$ direction. Simulated HAADF images of bulk SRO and GSO with orthorhombic structures are also inserted in the image. b) HAADF intensity profiles of A-site (left side) and B-site (right side) cations across the heterointerface. The data were collected along the red and blue dashed lines for A- and B-site cationic rows in (a), respectively. In the profiles, Sr ($Z = 38$), Gd ($Z = 64$), Ru ($Z = 44$), and Sc ($Z = 21$) atomic columns are colored in green, purple, gray, and pink, respectively. The interface position is denoted by the orange dashed line. c) ABF image taken from the same region as the HAADF image (a). In the image, oxygen atoms are clearly visible as dark contrast, revealing the projected shape of each oxygen octahedron and the octahedral connection across the interface as indicated with red solid rectangles. The simulated ABF images of bulk SRO and GSO are also included.

in relaxation of the octahedral tilt in the strained SRO films. We also discovered close correlation between the film structure and the in-plane displacement of apical oxygen atom at the film/substrate interface. This indicates the significance of the interfacial oxygen displacement, which characterizes the connection angle between the octahedra at the interface, as a determining factor for the octahedral distortions in the film. We further demonstrated that the octahedral distortions can be manipulated by interface engineering of the oxygen displacement, which consequently enables us to control the structural and electronic properties of the strained films.

2. Results and Discussion

Figure 1 shows typical cross-sectional STEM images of the tetragonal SRO thin film (t-SRO; 23 nm-thick) on the GSO substrate. In the HAADF image (Figure 1a), no misfit dislocations are seen at the heterointerface, confirming coherent growth of the film on the substrate. The observed image contrast, which depends on the atomic number (*Z*-contrast),[28,29] is in close agreement with that of the inserted simulation images. Figure 1b shows the HAADF intensity profiles of the A- and B-site cations obtained from Figure 1a. At the heterointerface, we see significant changes in the intensity profiles, indicating that the substrate is terminated at the ScO_2 layer[30] and that the t-SRO film begins with the SrO layer. The same cation arrangement at the interface is also seen for the monoclinic SRO thin film (m-SRO; 15 nm-thick) on the GSO substrate.[14] Figure 1c displays the ABF image taken from where the HAADF image was acquired (Figure 1a). In the ABF image, where the constituent atoms are observed as dark contrast,[31–33] we can clearly see not only the cation but also oxygen atomic columns, providing projected shapes of the octahedra. This is also verified from the inserted simulation images.

Figure 2 shows the out-of-plane lattice spacing and oxygen octahedral tilt angle of the m-SRO (Figure 2a) and t-SRO films (Figure 2b). The lattice spacing and tilt angle were extracted from the A-site cation positions in the HAADF images and the oxygen atomic positions in the ABF images, respectively. The definitions of the out-of-plane ($\theta_{out} < 180°$) and in-plane octahedral tilt angles ($\theta_{in} < 180°$) are given in Figure 2a. The bulk counterparts for the pseudocubic lattice spacing and tilt angle of the SRO (a_{pc} = 3.92 Å, θ_{SRO} = 168°)[34] and GSO (a_{pc} = 3.96 Å, θ_{GSO} = 156°)[35] are indicated by green and purple lines in the figures, respectively. We found that the out-of-plane lattice spacing of the m-SRO film is slightly larger than that of the t-SRO film and that the out-of-plane and in-plane octahedral tilts of the t-SRO film are smaller than those for the m-SRO film. The increase in out-of-plane lattice spacing for m-SRO is also confirmed from histogram analysis where the averaged out-of-plane lattice spacings for the m-SRO and t-SRO films are 3.92 Å and 3.89 Å, respectively (Supporting Information, Figure S1). This is consistent with the thickness-dependent change in the lattice parameters of the films determined from the X-ray diffraction analysis.[2] We also note that the variation of the out-of-plane tilt angle exhibits essentially the same trend as that of the in-plane tilt angle, regardless of the structural phase of SRO films.

Based on these observations, we schematically show the distorted octahedra in the m-SRO and t-SRO films in Figure 2c. For the m-SRO film, both out-of-plane lattice spacing and tilt angle are comparable to those of the bulk SRO (a_{pc} = 3.92 Å and $\theta = 168°$). Thus, the octahedra are distorted in such a way that they are stretched only along the in-plane direction and the bulk-equivalent tilt is accommodated. On the other hand, for the t-SRO film, the out-of-plane lattice spacing is reduced compared to the bulk and the octahedral tilt is largely suppressed. While the present ABF-STEM observations indicate the existence of tiny tilts, the octahedra in t-SRO can be regarded to be shrunk along the out-of-plane direction due to the tensile strain. The above observations therefore indicate that the monoclinic-to-tetragonal structural phase transition taking place at

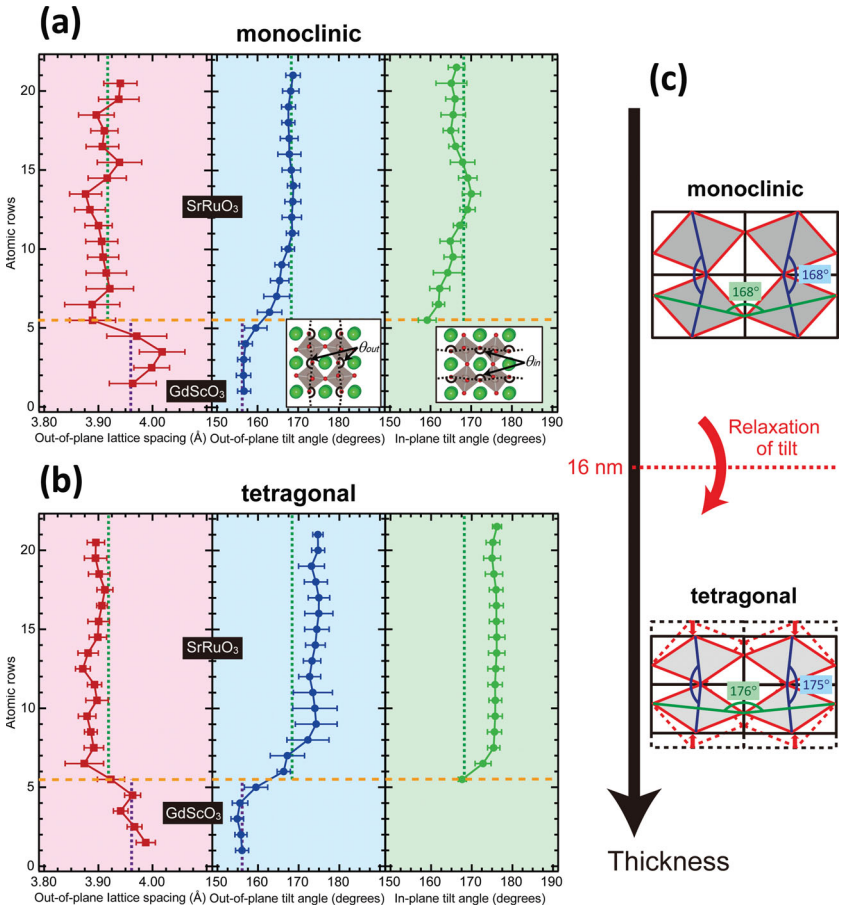

Figure 2. Quantitative analysis of octahedral distortions in SRO/GSO heterostructures. Variations in the out-of-plane lattice spacing (red) and out-of-plane (blue) and in-plane octahedral tilt angles (green) in the a) monoclinic and b) tetragonal SRO films on the GSO substrates. The out-of-plane lattice spacing and octahedral tilt angle were extracted from the HAADF and ABF images, respectively. The bulk counterparts for the pseudocubic lattice spacing and tilt angle of the SRO (a_{pc} = 3.92 Å, θ_{SRO} = 168°)[34] and GSO (a_{pc} = 3.96 Å, θ_{GSO} = 156°)[35] are indicated by green and purple lines, respectively. The tilt angle used in this study corresponds to the value projected along the $[001]_{ortho}$ direction. The orange dashed line represents the position of the SRO/GSO interface. The definition of the out-of-plane (θ_{out}) and in-plane octahedral tilt angles (θ_{in}) are shown in (a). c) Schematic drawings of the distorted RuO_6 octahedra in the monoclinic and tetragonal SRO films.

the 16 nm thickness[2] in the SRO films originates from the relaxation in the substrate-induced octahedral tilt. Both the m-SRO and t-SRO films are fully affected by substrate-induced tensile strain. In addition to the tensile strain, there are distortions by the induced octahedral tilt depending on the film thickness. Considering that the out-of-plane lattice spacing of m-SRO is larger than that of the t-SRO film under the same tensile strain, the lattice can accommodate the energy increased by the substrate-induced octahedral tilt up to 16 nm, although the m-SRO structure with the bulk-equivalent tilt is energetically unfavorable. For the films thicker than 16 nm, the lattice is no longer tolerant for accumulation of the additional energy and it relaxes to t-SRO by changing the octahedral tilt angle.

We also found that the relaxation of the octahedral tilt in the strained films gives rise to concomitant changes in octahedral connections across the heterointerface. **Figure 3**a plots the in-plane displacement Δx of the apical oxygen atom, which is directly related to the octahedral tilt. The definition of Δx is shown in the figure. For the m-SRO film, Δx of the apical oxygen atom away from the interface is almost comparable to the bulk value (21 pm), while for t-SRO, Δx is about 9 pm smaller than that of m-SRO. This is consistent with the above observations of the octahedral tilt (Figure 2). We note that the interfacial octahedral connections are also different for the two heterostructures, as depicted in Figure 3b. For the m-SRO/GSO heterostructure, the oxygen shared by the RuO_6 and ScO_6 octahedra at the interface has Δx of 26 pm, which is larger than that for the m-SRO film region away from the interface. As a result, the four RuO_6 octahedral layers above the topmost ScO_6 contribute to accommodate the difference in the octahedral tilt angle between the film and the substrate. For t-SRO/GSO, on the other hand, Δx at the interface is reduced to 19 pm and a single RuO_6 octahedral layer is sufficient for accommodating the difference in the tilt angle. Whereas the difference in the tilt angle or the oxygen displacement between the film and the substrate is larger for the t-SRO/GSO heterostructure than that for m-SRO/GSO, the number of octahedral layers necessary for accommodating the difference is less for t-SRO/GSO than for m-SRO/GSO. Thus, for the t-SRO/GSO heterostructure, propagation of the octahedral tilt from the substrate is blocked at the interface and the tilt angle relaxes to ≈175° in the film. We conclude that the interfacial octahedral connection, characterized by the displacement of the oxygen between RuO_6 and ScO_6 (highlighted with yellow boxes in Figure 3), is closely linked to the structural phases of the SRO films. Similar octahedral connections are also confirmed from the tilt angle measured along the in-plane direction (Figure 2).

We further demonstrated that the interface engineering of the oxygen displacement can manipulate the octahedral distortions and thus can be used as a tool to control the structural and electronic properties of the films. For perovskite oxides ABO_3, the in-plane displacement of the apical oxygen atom can be controlled by adjusting the octahedral tilt angle through the relative size mismatch between the A-site and B-site cations. According to the Goldschmidt tolerance factor prediction,[17,36–38] the relatively large A-site cation stabilizes the non-tilted octahedra. Based on this, we inserted the three unit-cell-thick $BaTiO_3$ (BTO) layer between the SRO film and GSO substrate to control oxygen displacement at the interface. In BTO, the relatively large ionic radius of Ba^{2+} (1.61 Å for 12 coordination) compared to Ti^{4+} (0.605 Å for 6 coordination) stabilizes the non-tilted TiO_6 octahedra. **Figure 4** represents cross-sectional STEM images of the SRO (10 nm)/BTO (1.2 nm)/GSO heterostructure. The

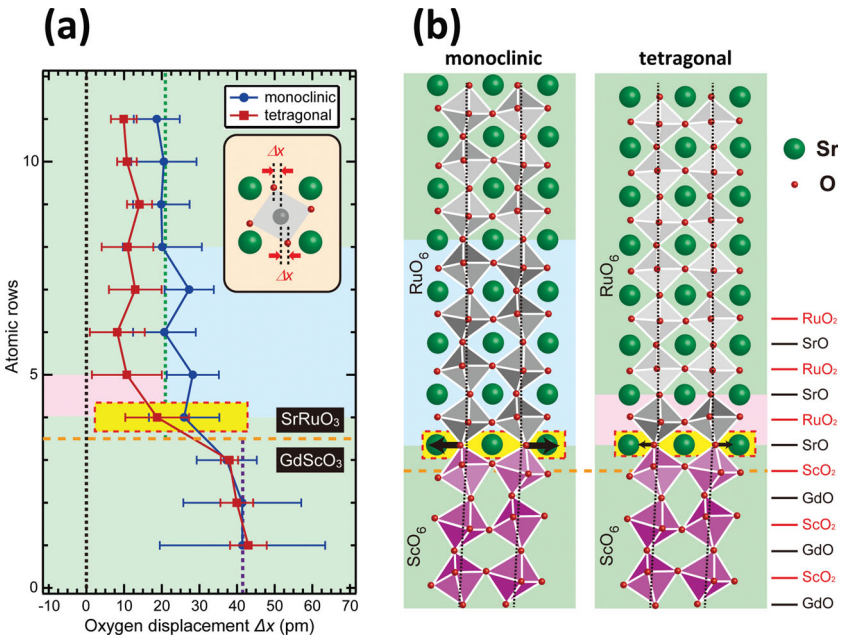

Figure 3. Atomic-scale structural characterization at SRO/GSO heterointerface. a) Variations of in-plane oxygen displacement in the monoclinic and tetragonal SRO/GSO heterostructures. The oxygen displacement Δx is defined as the distance from the middle position between A-site cations along the in-plane direction and was extracted from the ABF images. The oxygen displacements in bulk SRO (21 pm) and GSO (43 pm) are also shown with green and purple dotted lines, respectively. The blue and red boxes in the vicinity of the heterointerfaces represent the octahedral layers necessary to accommodate the difference in the tilt angle between the film and substrate regions for the monoclinic and tetragonal SRO films, respectively. b) Schematic drawings of the octahedral connections across the SRO/GSO interfaces projected along the $[001]_{ortho}$ direction. Whereas the in-plane lattice spacing for both monoclinic and tetragonal SRO films is identical to that of the GSO substrates, the in-plane oxygen displacement Δx at the SRO/GSO interface depends on the film structures as highlighted with the yellow boxes.

HAADF- (Figure 4a) and ABF-STEM images (Figure 4c) confirm coherent growth of the SRO and BTO layers without any misfit dislocations at each interface. We note that the in-plane lattice spacings for the SRO and BTO layers are identical to that of the GSO substrate (Supporting Information, Figure S2a). This is also corroborated by the results of the X-ray diffraction reciprocal space mapping (Supporting Information, Figure S3). The HAADF intensity profiles in Figure 4b indicate that B-site terminations are preserved at each SRO/BTO and BTO/GSO interface. These observations ensure the designed growth of the high-quality SRO/BTO/GSO heterostructure.

Figure 5a plots the variations in the out-of-plane lattice spacing and octahedral tilt angle as a function of the atomic position in the SRO/BTO/GSO heterostructure. The BTO layer has out-of-plane lattice spacing slightly larger than the bulk due to compressive strain (–0.8%). Strong suppression in the octahedral tilt angle across the BTO/GSO interface is seen; the tilt angle changes from 156° in the substrate region to 180° in the three unit-cell-thick BTO layer. Consequently, the tilt angle at the interface between the SRO and BTO layers becomes 180°, stabilizing the RuO_6-TiO_6 octahedral connection with the negligible tilts. In the SRO layer on BTO/GSO, the out-of-plane lattice spacing is slightly reduced from the bulk and is 3.90 Å (Supporting Information, Figure S2b), comparable to that of the above t-SRO/GSO heterostructure. These observations indicate that the SRO layer grown on BTO/GSO has a structure very close to that of the t-SRO film on GSO. It should be emphasized that the thickness of the SRO film on the BTO/GSO is below the critical thickness of the octahedral tilt relaxation (16 nm) and that the SRO film with a similar film thickness grown directly on the GSO substrate has a monoclinic structure as shown above.

The behavior of the octahedral tilt in the SRO/BTO/GSO heterostructure is also confirmed from the in-plane displacement Δx of the apical oxygen atom (Figure 5b). We see that Δx is significantly reduced at the BTO/GSO interface and decreases to 0 pm within the three unit-cell-thick BTO layer, meaning zero in-plane displacement of the oxygen shared by RuO_6 and TiO_6 at the interface (highlighted with yellow boxes in Figure 5b,c). Based on these observations, the octahedral connections in the heterostructure are schematically shown in Figure 5c. It is clear that the octahedral tilt from the GSO substrate does not propagate to the SRO layer by the insertion of the three unit-cell-thick BTO layer which stabilizes the RuO_6-TiO_6 octahedral connection with the negligible tilts. Thus, we conclude that the octahedral distortions in the SRO film can also be manipulated by adjusting the RuO_6-TiO_6 octahedral connection through the in-plane displacement of the apical oxygen atom at the interface.

Figure 6 summarizes the magnetotransport properties of the SRO layer grown on BTO/GSO, revealing the strong impact of the interfacial engineering of the oxygen displacement on the spin-orbit coupling in the SRO layer. Figure 6a shows the temperature dependence of the longitudinal resistivity ρ_{xx} for SRO/BTO/GSO. As in the case of the SRO/GSO heterostructures, the SRO/BTO/GSO heterostructure exhibits metallic conduction down to 10 K and undergoes a ferromagnetic transition at 113 K, which can be seen as a hump in the ρ_{xx}–T curve. The magnetic ordering in SRO/BTO/GSO is also confirmed by the anomalous Hall effect seen in the magnetic field dependence of the transverse Hall resistivity ρ_{xy} at 10 K (Figure 6b). The anomalous Hall effect for the SRO layer grown on BTO/GSO is characteristic with in-plane magnetic anisotropy in contrast to that observed for the m-SRO/GSO. To further determine the magnetic easy axis direction in the SRO/BTO/GSO, we also measured the magnetic field angle θ_H dependence of ρ_{xx} and ρ_{xy} for various configurations of the applied current and field directions at 10 K. The results are shown in Figure 6c–e. Due to the strong magnetic anisotropy of SRO,[2,3] reversal of the magnetic moment takes place when the angle between the easy axis and the field exceeds 90°. This can be observed as peaks in ρ_{xx} and jumps in ρ_{xy}.[2,3] Indeed, field-induced reversal of the magnetic moment is seen every 180° in θ_H when the field rotates in the $(001)_{ortho}$ (Figure 6d) and $(110)_{ortho}$ plane (Figure 6e). This indicates that the SRO layer on

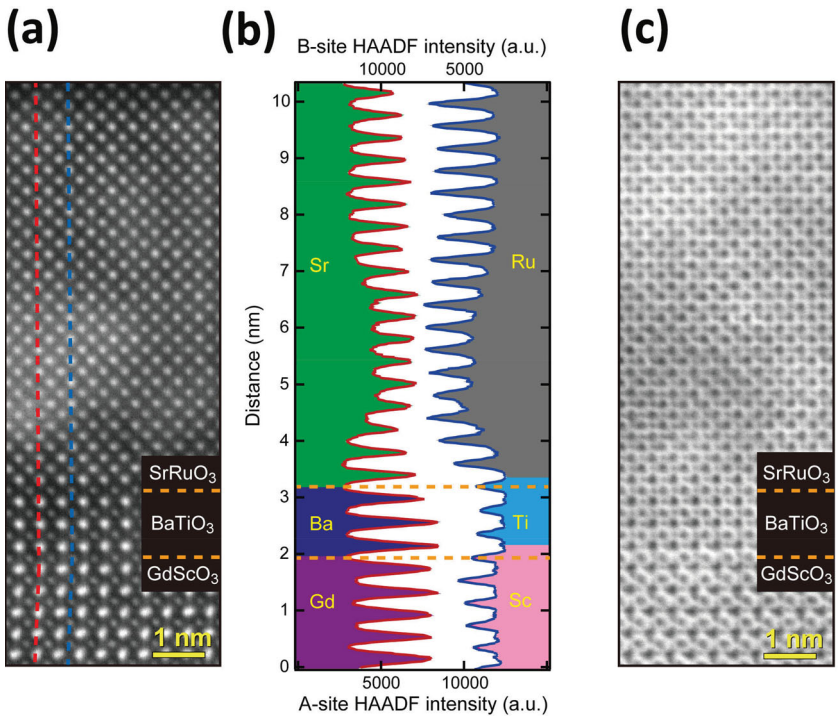

Figure 4. High-resolution cross-sectional HAADF- and ABF-STEM images of the SRO (10 nm)/BTO (1.2 nm)/GSO heterostructure and element characterization. a) High-resolution HAADF image of the SRO/BTO/GSO heterostructure taken along the $[001]_{ortho}$ direction. b) HAADF intensity profiles of A-site (left side) and B-site (right side) cations across the heterointerface. The data were collected along the red and blue dashed lines for A- and B-site cationic rows in (a), respectively. In the profiles, Sr ($Z = 38$), Ba ($Z = 56$), Gd ($Z = 64$), Ru ($Z = 44$), Ti ($Z = 22$), and Sc ($Z = 21$) atomic columns are colored in green, blue, purple, gray, cyan, and pink, respectively. c) ABF image taken from the same region as the HAADF image (a). The interface position is denoted by the orange dashed line.

BTO/GSO has uniaxial magnetic anisotropy with the easy axis parallel to the $[1\text{–}10]_{ortho}$ direction, which is the same as t-SRO on GSO.[2,3] We also note that as shown in Figure 6f, the easy axis direction of the SRO layer on BTO/GSO is temperature independent. Given the close correlation between the magnetic anisotropy and the RuO_6 octahedral distortions in SRO,[2,3] the observed magnetotransport properties in Figure 6 lead to the conclusion that the SRO layer on BTO/GSO is in the tetragonal phase, not the monoclinic one. The results demonstrate that the structural and electronic properties in the SRO films can be controlled through the octahedral connection adjusted by manipulating the displacement of the apical oxygen atom at the interface.

3. Conclusions

We investigated octahedral distortions in strained SRO films grown on GSO substrates by precisely determining atomic positions for all constituent elements, including oxygen from high-resolution HAADF- and ABF-STEM observations. We found that the monoclinic (film thickness less than 16 nm) and tetragonal (more than 16 nm) structural phases of the SRO film are characterized by the difference in the octahedral

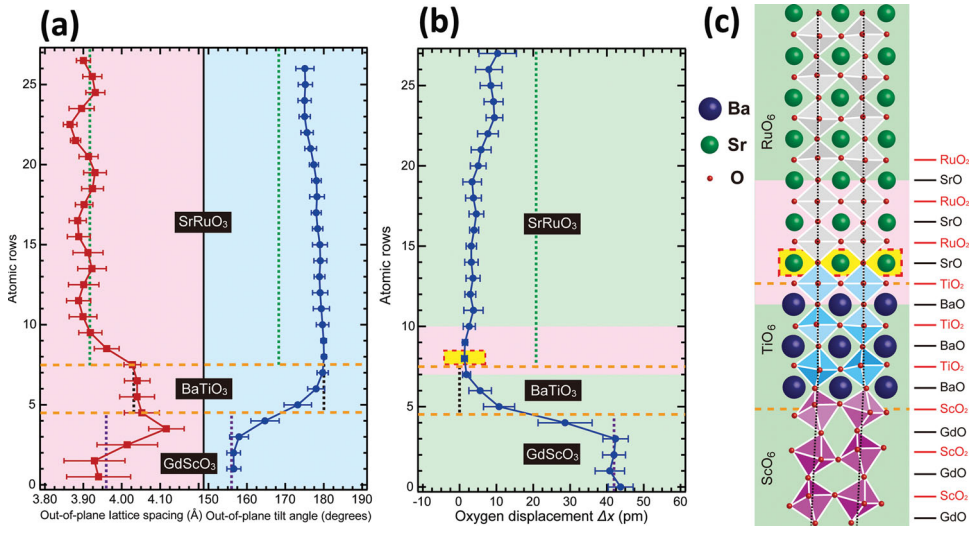

Figure 5. Control of octahedral distortion in the SRO film by interfacial engineering of the oxygen displacement. a) Variations of the out-of-plane lattice spacing (red) and octahedral tilt angle (blue) in the SRO/BTO/GSO heterostructure. The out-of-plane lattice spacing and tilt angle were extracted from the corresponding HAADF and ABF images, respectively. The bulk counterparts for the out-of-plane pseudocubic lattice spacing and tilt angle of the SRO, BTO ($a_{pc} = 4.03$ Å, $\theta_{BTO} = 180°$), and GSO are indicated by the green, black, and purple dotted lines, respectively. b) Variation of the in-plane oxygen displacement Δx extracted from the ABF image of the SRO/BTO/GSO heterostructure. The Δx of the bulk SRO (21 pm, green), BTO (0 pm, black), and GSO (43 pm, purple) are also shown in the graph. c) Schematic drawings of the octahedral connections in the SRO/BTO/GSO heterostructure projected along the $[001]_{ortho}$ direction. The octahedral tilt is heavily reduced (red region) and the tilt angle is 180° at the SRO/BTO interface, as highlighted with the yellow box. The orange dashed lines also represent the SRO/BTO and SRO/GSO interfaces.

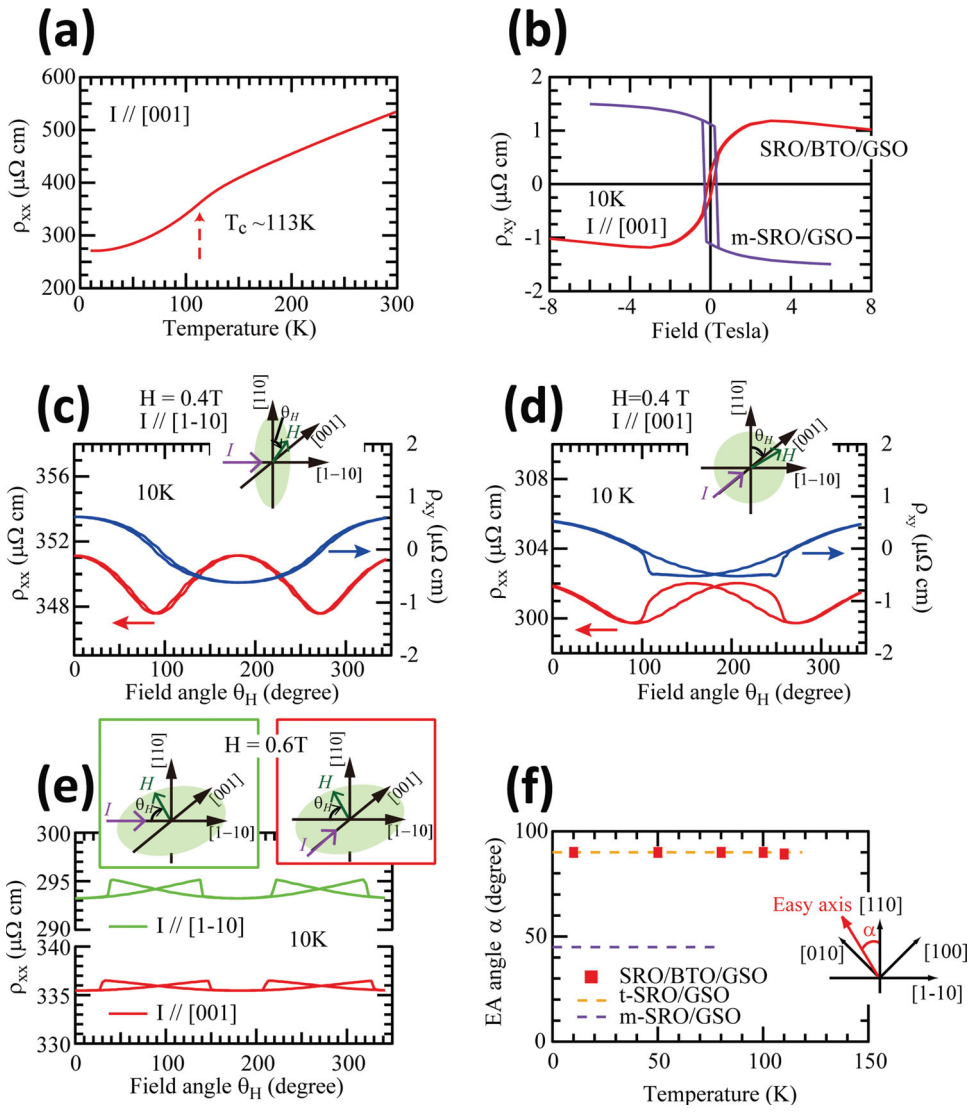

Figure 6. Transport properties of the tetragonal SRO phase stabilized by interface engineering of the oxygen displacement. a) Temperature dependence of longitudinal resistivity ρ_{xx} of the 10 nm-thick SRO film on BTO (1.2 nm)/GSO. b) Magnetic field dependence of Hall resistivity ρ_{xy} at 10 K. As a reference, the field dependence of ρ_{xy} for the monoclinic SRO film directly grown on the GSO substrate is also shown. c–e) Magnetic field angle θ_H dependence of ρ_{xx} and ρ_{xy} with various current and field configurations measured at 10 K. In (c), the field was rotated in the $(1\text{–}10)_{ortho}$ plane and current was applied along the $[1\text{–}10]_{ortho}$ direction. In (d), the field was rotated in the $(001)_{ortho}$ plane and current was applied along the $[001]_{ortho}$ direction. In (e), the field was rotated in the $(110)_{ortho}$ plane. The current flowed along the $[1\text{–}10]_{ortho}$ (the upper plot) and $[001]_{ortho}$ directions (the lower plot). The index is based on the orthorhombic perovskite notation. f) Temperature dependence of the magnetic easy axis (EA) angle α of the SRO layer on BTO/GSO. The direction of the magnetic easy axis was determined from the magnetic field angle θ_H dependence of ρ_{xx}. The EA angles for m-SRO and t-SRO were taken from our previous studies[2,3] where the thickness- and temperature-independence of the EA angle α for m-SRO/GSO and t-SRO/GSO were established.

distortions associated with the tilt relaxation. The finding of close correlation between the film structure and the in-plane displacement of the apical oxygen atom at the interface leads us to the idea of controlling octahedral distortions in the SRO film by inserting the three unit-cell-thick BTO layer between the SRO layer and the GSO substrate. In the SRO/BTO/GSO heterostructure, the tetragonal phase of the SRO layer is stabilized even with the film thickness for which the monoclinic phase is seen without the BTO layer. Our results demonstrate that the manipulation of the oxygen displacement at the heterointerface is a good way to control structural and electronic properties in strained perovskite oxide films and provides a further degree of freedom for designing novel oxide-based heterostructures.

4. Experimental Section

$SrRuO_3$ (SRO) and $BaTiO_3$ (BTO) film layers were epitaxially grown on $(110)_{ortho}$ $GdScO_3$ (GSO) substrates by pulsed laser deposition. For the indexes, the subscripts "pc" and "ortho" denote the pseudocubic and orthorhombic perovskite notation, respectively. Details of the thin film fabrication process are given in our previous report.[2,39] Briefly, during film growth, the substrate temperature was fixed at 700 °C.

The oxygen pressure was set to be 100 and 25 mTorr, respectively, for the SRO and BTO layer depositions. We performed X-ray diffraction to characterize the structural phases of the fabricated samples. We confirmed that all heterostructures used in this study were coherently grown on the substrates and that there were no crystallographic twins.[40] For the transport measurements, we used 50 μm-wide Hall-bar samples fabricated by conventional photolithography and Ar-ion milling. The longitudinal and transverse Hall resistivities were measured in a conventional four-terminal configuration with a Physical Property Measurement System (PPMS, Quantum Design) equipped with a sample rotator.

For the cross-sectional STEM observations, the thin film specimens were thinned down to electron transparency by mechanical polishing and Ar-ion milling.[41] STEM images were acquired at room temperature in a spherical aberration corrected STEM (JEM-9980TKP1; accelerating voltage = 200 kV, C_s = –0.025 mm, C_5 = 15 mm) equipped with a cold field emission gun. The annular detection angle for the HAADF imaging was 50–133 mrad and that for the ABF imaging was 11–23 mrad, since the convergent semi-angle of the incident probe was 23 mrad. 50 HAADF and 50 ABF images were acquired from the same area with a short dwell time (≈ 4.2 μs per pixel). Multiple images were then superimposed after correcting for relative drifts.[42] This procedure provides high-resolution STEM images with an improved signal-to-noise (SN) ratio and minimized image distortion. Measurements of the atomic positions in the STEM images were carried out at sub-pixel resolution using Bragg filtering and cubic interpolation techniques in the "Find Peaks" option (Peak Pairs Analysis software package by HREM Research).[43,44] The lattice spacing was determined from the average over 18 unit cells of the pseudocubic perovskite lattice layer along the $[1\text{–}10]_{ortho}$ direction (the in-plane direction) in the HAADF images. The tilt angle θ of the oxygen octahedra along the $[110]_{ortho}$ direction was also determined by averaging alternately over 18 unit cells of the pseudocubic perovskite lattice layer along the $[1\text{–}10]_{ortho}$ direction.

The HAADF and ABF images were simulated using the multislice simulation software (WinHREM by HREM Research). The optical parameters used for the simulations were the same as the experimentally obtained values. The image simulations were carried out for bulk structures of SRO and GSO.

Supporting Information

Supporting Information is available from the Wiley Online Library or from the author.

Acknowledgements

This work was partially supported by a Grant-in-Aid for Scientific Research (Grant No. 24760009), and a grant for the Joint Project of Chemical Synthesis Core Research Institutions from the Ministry of Education, Culture, Sports, Science and Technology of Japan. The work was also supported by the Japan Science and Technology Agency, CREST.

Received: October 14, 2013
Revised: January 11, 2014
Published online: April 25, 2014

[1] Y. W. Yin, J. D. Burton, Y-M. Kim, A. Y. Borisevich, S. J. Pennycook, S. M. Yang, T. W. Noh, A. Gruverman, X. G. Li, E. Y. Tsymbal, Q. Li, *Nat. Mater.* **2013**, *12*, 397.
[2] D. Kan, R. Aso, H. Kurata, Y. Shimakawa, *Adv. Funct. Mater.* **2013**, *23*, 1129.
[3] D. Kan, R. Aso, H. Kurata, Y. Shimakawa, *J. Appl. Phys.* **2013**, *113*, 173912.
[4] F. Sandiumenge, J. Santiso, L. Balcells, Z. Konstantinovic, J. Roqueta, A. Pomar, J. P. Espinós, B. Martínez, *Phys. Rev. Lett.* **2013**, *110*, 107206.
[5] H. Y. Hwang, Y. Iwasa, M. Kawasaki, B. Keimer, N. Nagaosa, Y. Tokura, *Nat. Mater.* **2012**, *11*, 103.
[6] C. Cantoni, J. Gazquez, F. M. Granozio, M. P. Oxley, M. Varela, A. R. Lupini, S. J. Pennycook, C. Aruta, U. S. D. Uccio, P. Perna, D. Maccariello, *Adv. Mater.* **2012**, *24*, 3952.
[7] H. Lu, X. Liu, J. D. Burton, C.-W. Bark, Y. Wang, Y. Zhang, D. J. Kim, A. Stamm, P. Lukashev, D. A. Felker, C. M. Folkman, P. Gao, M. S. Rzchowski, X. Q. Pan, C.-B. Eom, E. Y. Tsymbal, A. Gruverman, *Adv. Mater.* **2012**, *24*, 1209.
[8] J. H. Lee, L. Fang, E. Vlahos, X. Ke, Y. W. Jung, L. F. Kourkoutis, J.-W. Kim, P. J. Ryan, T. Heeg, M. Roeckerath, V. Goian, M. Bernhagen, R. Uecker, P. C. Hammel, K. M. Rabe, S. Kamba, J. Schubert, J. W. Feeland, D. A. Muller, C. J. Fennie, P. Schiffer, V. Gopalan, E. J. Halperin, D. G. Schlom, *Nature* **2010**, *466*, 954.
[9] J. He, A. Borisevich, S. V. Kalinin, S. J. Pennycook, S. T. Pantelides, *Phys. Rev. Lett.* **2010**, *105*, 227203.
[10] A. Y. Borisevich, H. J. Chang, M. Huijben, M. P. Oxley, S. Okamoto, M. K. Niranjan, J. D. Burton, E. Y. Tsymbal, Y. H. Chu, P. Yu, R. Ramesh, S. V. Kalinin, S. J. Pebnnycook, *Phys. Rev. Lett.* **2010**, *105*, 087204.
[11] A. T. Zayak, X. Huang, J. B. Neaton, K. M. Rabe, *Phys. Rev. B* **2008**, *77*, 214410.
[12] A. T. Zayak, X. Huang, J. B. Neaton, K. M. Rabe, *Phys. Rev. B* **2006**, *74*, 094104.
[13] H. N. Lee, H. M. Christen, M. F. Chisholm, C. M. Rouleau, D. H. Lowndes, *Nature* **2005**, *433*, 395.
[14] R. Aso, D. Kan, Y. Shimakawa, H. Kurata, *Sci. Rep.* **2013**, *3*, 2214.
[15] S. H. Chang, Y. J. Chang, S. Y. Jang, D. W. Jeong, C. U. Jung, Y.-J. Kim, J.-S. Chung, T. W. Noh, *Phys. Rev. B* **2011**, *84*, 104101.
[16] S. J. May, C. R. Smith, J.-W. Kim, E. Karapetrova, A. Bhattacharya, P. J. Ryan, *Phys. Rev. B* **2011**, *83*, 153411.
[17] A. Vailionis, H. Boschker, W. Siemons, E. P. Houwman, D. H. A. Blank, G. Rijnders, G. Koster, *Phys. Rev. B* **2011**, *83*, 064101.
[18] D. Kan, Y. Shimakawa, *Cryst. Growth Des.* **2011**, *11*, 5483.
[19] C. L. Jia, S. B. Mi, M. Faley, U. Poppe, J. Schubert, K. Urban, *Phys. Rev. B* **2009**, *79*, 081405(R).
[20] A. Ohtomo, H. Y. Hwang, *Nature* **2004**, *427*, 423.
[21] K. J. Choi, M. Biegalski, Y. L. Li, A. Sharan, J. Schubert, R. Uecker, P. Reiche, Y. B. Chen, X. Q. Pan, V. Gopalan, L.-Q. Chen, D. G. Schlom, C. B. Eom, *Science* **2004**, *306*, 1005.
[22] J. M. Rondinelli, S. J. May, J. W. Freeland, *MRS Bulletin* **2012**, *37*, 261.
[23] J. M. Rondinelli, N. A. Spaldin, *Adv. Mater.* **2011**, *23*, 3363.
[24] J. M. Rondinelli, S. Coh, *Phys. Rev. Lett.* **2011**, *106*, 235502.
[25] A. J. Hatt, N. A. Spaldin, *Phys. Rev. B* **2010**, *82*, 195402.
[26] J. M. Rondinelli, N. A. Spaldin, *Phys. Rev. B* **2010**, *82*, 113402.
[27] S. J. May, J.-W. Kim, J. M. Rondinelli, E. Karapetrova, N. A. Spaldin, A. Bhattacharya, P. J. Ryan, *Phys. Rev. B* **2010**, *82*, 014110.
[28] S. J. Pennycook, D. E. Jesson, *Ultramicroscopy* **1991**, *37*, 14.
[29] S. J. Pennycook, D. E. Jesson, *Phys. Rev. Lett.* **1990**, *64*, 938.
[30] J. E. Kleibeuker, G. Koster, W. Siemons, D. Dubbink, B. Kuiper, J. L. Blok, C.-H. Yang, J. Ravichandran, R. Ramesh, J. E. T. Elshof, D. H. A. Blank, G. Rijnders, *Adv. Funct. Mater.* **2010**, *20*, 3490.
[31] M. Haruta, H. Kurata, *Sci. Rep.* **2012**, *2*, 252.
[32] S. D. Findlay, N. Shibata, H. Sawada, E. Okunishi, Y. Kondo, Y. Ikuhara, *Ultramicroscopy* **2010**, *110*, 903.
[33] S. D. Findlay, N. Shibata, H. Sawada, E. Okunishi, Y. Kondo, T. Yamamoto, Y. Ikuhara, *Appl. Phys. Lett.* **2009**, *95*, 191913.
[34] C. W. Jones, P. D. Battle, P. Lightfoot, *Acta Cryst. C* **1989**, *45*, 365.
[35] R. P. Liferovich, R. H. Mitchell, *J. Solid State Chem.* **2004**, *177*, 2188.

[36] J. B. Goodenough, *Rep. Prog. Phys.* **2004**, *67*, 1915.
[37] P. M. Woodward, *Acta Cryst. B* **1997**, *53*, 32.
[38] P. M. Woodward, *Acta Cryst. B* **1997**, *53*, 44.
[39] D. Kan, Y. Shimakawa, *Appl. Phys. Lett.* **2011**, *99*, 081907.
[40] D. Kan, Y. Shimakawa, *J. Appl. Phys.* **2012**, *111*, 093532.
[41] L. Dieterle, B. Butz, E. Müller, *Ultramicroscopy* **2011**, *111*, 1636.
[42] M. Saito, K. Kimoto, T. Nagai, S. Fukushima, D. Akahoshi, H. Kuwahara, Y. Matsui, K. Ishizuka, *J. Electron Microscop.* **2009**, *58*, 131.
[43] P. Galindo, J. Pizarro, S. Molina, K. Ishizuka, *Microsc. Anal.* **2009**, *23*, 23.
[44] P. L. Galindo, S. Kret, A. M. Sanchez, J.-Y. Laval, A. Yáñez, J. Pizarro, E. Guerrero, T. Ben, S. I. Molina, *Ultramicroscopy* **2007**, *107*, 1186.